Thyroid Microwave Ablation Study Based on Fiber Bragg Gratings Thermal Mapping

Elena De Vita, *Member, IEEE*, Francesca De Tommasi, *Student Member, IEEE*, Carlo Altomare, Daniela Lo Presti, *Member, IEEE*, Giuseppina Pacella, Agostino Iadicicco, Massimiliano Carassiti, Rosario Francesco Grasso, Carlo Massaroni, *Senior Member, IEEE*, Stefania Campopiano, and Emiliano Schena, *Senior Member, IEEE*

***Abstract*—Thyroid nodules represent a widespread health concern and surgery is often adopted even if the incidence of frequent post-operative complications is not negligible. In recent years, this framework has fostered the growing spread of thermal ablation treatments, in particular microwave ablation (MWA). To date, despite its relevance, state-of-the-art regarding temperature monitoring in thyroid tissue during MWA is lacking. In this paper, the effects of MWA in thyroid by monitoring temperatures have been explored. By using several fiber Bragg gratings (FBGs) temperature sensors, the heat maps in the proximity of the MW antenna have been reconstructed for two different power values set at generator. An increase up to about 4.5 cm^3 in ablation volume and up to 24 °C in maximum temperature variation as power rises from 20 W to 30 W has been observed. In addition, the dependency of the temperature evolution on the involved power has been investigated, observing that, with increasing power, some FBGs recorded a ΔT slope increase until the maximum values, resulting in shorter ablation times, and others recorded a plateau phase until the end of the MWA treatment. Such a propensity could be relevant to adjust the clinical settings according to the desired treatment outcome.**

***Index Terms*—Fiber Bragg gratings, microwave ablation, temperature monitoring, thermal ablation, thyroid nodules.**

I. Introduction

OVER the past decades, thyroid nodules represent a widespread health concern encountered in up to 76% of the global population, whose burden grows with advancing age [1], [2], [3]. In 95% of occurrences, their nature is benign and asymptomatic, and only 5% are revealed malignant, demanding a pressing need for intervention [4], [5]. Nevertheless, surgery is often adopted even for benign neoplasms since pain and inconvenience in swallowing, hyperthyroidism, and aesthetic impairment appear recurrently [6]. Despite surgical procedures being nowadays recognized as the gold standard for the management of such lesions, the incidence of frequent post-operative complications is not negligible. Besides the evident disadvantages associated with this type of approach (e.g., long hospital stays, the risk of general anesthesia), a conspicuous number of patients face damage to the parathyroid glands, laryngeal nerve trauma or paralysis, neck hematoma, and unsightly scars [7], [8], [9], [10]. Such adverse repercussions hurt patients' quality of life and prompted an urgent demand for minimally invasive alternatives. In recent years, this framework has fostered the growing spread of thermal ablation (TA) treatments. Their clinical acceptability for dealing with thyroid nodules is also witnessed in guidelines laid down by scientific communities worldwide [1], [11], [12], [13]. Reduced procedural time, very brief hospital stays, early patient recovery, and low costs are the hallmarks of TA and enable their preference over conventional surgery. TA inflicts permanent damage to cancer tissue by applying extreme temperatures [14], [15]. Generally, thermal damage of an additional margin (ranging between 5 mm and 10 mm) around the neoplasm is also advisable, leaving neighboring healthy structures unharmed, but in the case of the thyroid gland, this is not necessary when treating benign lesions [16]. During TA, a quantity of energy is discharged and released inside the affected tissue through an applicator. Thus, the temperature rise process stems from the energy-tissue interplay and differs depending on the source employed [17].

Among different TA, microwave ablation (hereafter, MWA) ranks as one of the most promising. Its success in clinical practice arises from several benefits compared to other techniques (e.g., radiofrequency ablation – RFA – or laser ablation – LA), such as rapid heating even on a large tissue volume, low susceptibility to heat dissipation caused by blood perfusion, high temperatures and the possibility of using more than one applicator concurrently [14], [18]. The working principle of MWA lies in the interaction between water molecules and the externally applied electromagnetic field that forces dipoles to realign themselves with the oscillating electric field continuously. This phenomenon leads to an increase in kinetic energy and, thus, a rise in temperature inside the tissue [19]. During MWA and TA in general,

Manuscript received 18 September 2023; revised 28 December 2023; accepted 13 January 2024. Date of publication 8 February 2024; date of current version 1 March 2024. This work was supported by the Italian Ministry of Education and Research through the Project "More Care," CUP: I63C21000250006, under PRIN 2020 Grant. *(Corresponding author: Stefania Campopiano.)*

Elena De Vita, Agostino Iadicicco, and Stefania Campopiano are with the Department of Engineering, University of Naples "Parthenope", 80143 Naples, Italy (e-mail: elena.devita@collaboratore.uniparthenope.it; agostino.iadicicco@uniparthenope.it; stefania.campopiano@uniparthenope.it).

Francesca De Tommasi, Daniela Lo Presti, Carlo Massaroni, and Emiliano Schena are with the Department of Engineering, Università Campus Bio-Medico di Roma, 00128 Rome, Italy (e-mail: f.detommasi@unicampus.it; d.lopresti@unicampus.it; c.massaroni@unicampus.it; e.schena@unicampus.it).

Carlo Altomare, Giuseppina Pacella, Massimiliano Carassiti, and Rosario Francesco Grasso are with the School of Medicine, Università Campus Bio-Medico di Roma, 00128 Rome, Italy (e-mail: c.altomare@policlinicocampus.it; g.pacella@policlinicocampus.it; m.carassiti@policlinicocampus.it; r.grasso@policlinicocampus.it).

Digital Object Identifier 10.1109/JERM.2024.3358991

temperature monitoring may hold a key role as the amount of injured volume is strongly dependent on temperature values and their permanence time [20]. Thus, gathering temperature information would be beneficial to find the proper treatment settings and achieve the optimal match between the cancerous volume and the damaged one, which remains an open challenge to date. Indeed, clinicians perform the procedure without any real-time feedback regarding the amount of injury. Therefore, incomplete ablation or damage to healthy structures is often recurrent. For this reason, various solutions have been proposed to keep track of temperatures during TA [21], [22]. Among others, fiber Bragg grating sensors (hereafter FBGs) emerge as one of the most promising solutions in this field [23], [24], [25], [26]. Along with the well-known merits of fiber optic sensors in general (e.g., biocompatibility, small dimensions, immunity to electromagnetic interferences), the ability of FBGs to be multiplexed within a single optical fiber allows for easily gathering temperature tissue maps with high spatial resolution and good accuracy, favoring them over other electrical sensors.

To date, despite its relevance, state-of-the-art regarding temperature monitoring in thyroid tissue during MWA is lacking. Studies found in the literature only come from clinical sources and evaluate the feasibility and effectiveness of this technique by following up with patients and tracking the occurrence of complications after treatment [27], [28], [29], [30], [31].

To fill this knowledge gap, this article presents the first investigation of temperature in ex vivo thyroid tissue during MWA. Temperature measurements were accomplished by means of two optical fibers, each one embedding ten FBGs for a total of twenty measuring points. This approach allowed to gain spatial and temporal temperature distribution around the MW applicator and analyze its changes according to the different treatment settings generally employed in clinical practice. A preliminary version of this work was reported in a conference proceeding [32]. In the current one, we extended our research by *i)* analyzing different settings, *ii)* assessing the size of necrosis area and its shape after treatment, *iii)* comparing the temperature variations recorded by FBGs with those retrieved by the thermocouples embedded in the MW applicator, and *iv)* providing heat maps for each trial carried out. In the following, the experimental setup employed to perform the tests of MWA on ex vivo thyroid samples is reported, and the results in terms of ablation volumes and temperature measurements are discussed.

II. Materials and Methods

This section is devoted to the description of the sensors and the other instruments deployed for performing and monitoring the MWA tests. Therefore, the sensing principle of FBGs is illustrated, and each experimental setup component is detailed hereafter.

A. Working Principle of the FBGs

Contrary to usual optical fibers, characterized by a constant refractive index of the core, the FBG core is periodically perturbed along the direction of the light propagation. Such perturbation is called grating and enables the light backward reflection besides the input light transmission along the fiber. More specifically, in correspondence of an FBG, the narrow band of the input light centered around the specific wavelength λ_{B} (i.e., Bragg wavelength), feature of that FBG, is reflected while the remaining wavelengths are transmitted without disturbances. The expression of λ_{B} is given by [33]:

$$\lambda_B = 2n_{eff}\Lambda \tag{1}$$

so that the reflected wavelength λ_{B} depends on the grating period Λ and the effective refractive index n_{eff} of the core mode, both acting as sensor inputs. Indeed, λ_{B} represents the measured quantity, whereas the parameters which affect and change Λ and n_{eff} are the measurands.

Therefore, the sensing principle of the FBG lies in the measurement of the λ_{B} shift caused by changes of Λ and n_{eff}, which in turn are typically affected by strain (ε) and temperature variations (ΔT) occurring around the fiber. The expression of the normalized λ_{B} shift is given by [33], [34]:

$$\frac{\Delta\lambda_B}{\lambda_B} = (\xi + \alpha)\ \Delta T + (1 - p_\varepsilon)\,\varepsilon \tag{2}$$

where the first addendum depends on ΔT through the thermo-optic and thermal expansion coefficients ξ and α, respectively, whereas the second one depends on the strain ε through the strain factor p_ε. Assuming no strain acting on the fiber, the λ_{B} shift depends only on the temperature contribution and (2) becomes:

$$\frac{\Delta\lambda_B}{\lambda_B} = S_T\ \Delta T \tag{3}$$

where S_T identifies the thermal sensitivity of the FBG equal to the sum of ξ and α.

The wavelength division multiplexing exhibited by FBGs makes them ideal for minimally invasive measurements with high spatial resolution. Indeed, for the measurements reported in this work, two arrays of ten FBGs each were employed in such a way that, by inserting only two optical fibers inside the thyroid tissue, twenty sensing points could be distributed nearby the MW applicator. Moreover, each FBG had a length of 1 mm and was spaced from the adjacent one of 2 mm for each array, resulting in a dense measurement area in a limited portion of tissue. Such high spatial resolution represents a key element for this application especially considering the very small size of thyroid lobes where MWA tests were performed.

Before starting with MWA experiments, the employed arrays were characterized, and a thermal sensitivity of approximately $6.5{\cdot}10^{-6}$ °C^{-1} was measured for each FBG. During the MWA tests, the Bragg wavelengths of the sensors were acquired by the optical interrogation unit, as described in the following, with resolution and accuracy of 1 pm and 2 pm, respectively. Therefore, temperature measurements exhibited a resolution of 0.1 °C and an accuracy of $\pm$ 0.2 °C.

The optical spectrum reflected by one of the involved arrays is reported in Fig. 1(a) before and after recording a temperature variation ranging from 9 °C to 54 °C among the FBGs of the array. It can be observed that the λ_{B} of each FBG is spaced of approximately 10 nm from each other, in such a way that the reflected wavelengths did not overlap in the optical spectrum

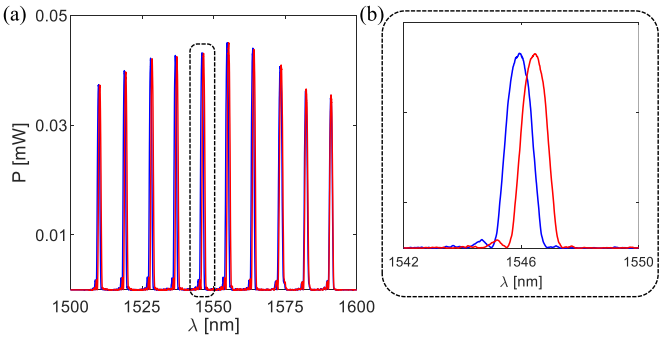

Fig. 1. Optical reflected spectrum by one of the employed arrays of FBGs before (in blue) and after (in red) a temperature variation (a), with a zoom in correspondence of the fifth FBG (b).

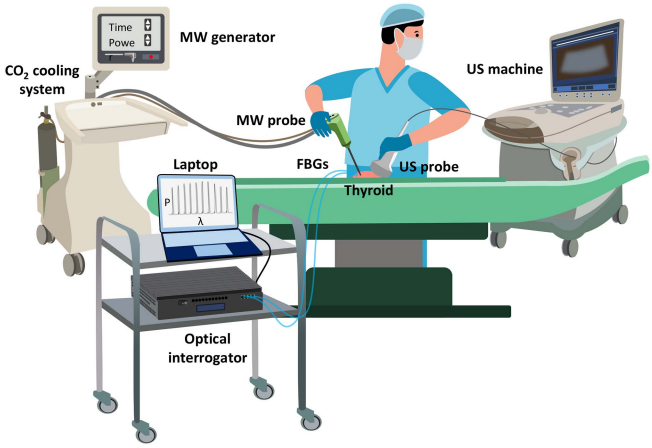

Fig. 2. Experimental setup employed during the MWA tests on thyroid tissue.

during the experiments. A zoom in correspondence of the fifth peak is reported in Fig. 1(b) for the sake of clarity.

B. Experimental Setup

The experiments were performed on fresh ex vivo lobes of swine thyroids extracted and collected immediately after animal sacrifice from a local slaughterhouse. As shown in Fig. 2, several instruments have been involved, including MWA, optical, and ultrasound equipment.

MWA was performed by means of MW generator and probe, Certus 140^{TM} and PR15 models, respectively, both by NeuWave Medical Inc. MWA equipment is represented on the left in Fig. 2. The generator was configured in the ablation mode and worked at a frequency of 2.45 GHz. The power output of the generator was set at 20 W and 30 W, whereas time duration was constant for all the performed tests and equal to 5 min. Indeed, one of the main goals of this work lies in the comparison of the MWA effects for different power values in order to investigate the power impact on the ablation outcomes. It is worth noting that usually along the power distribution system approximately the 30% of the power set at the generator dissipates due to coaxial cable losses [35]. Therefore, for the two power settings considered in this study, i.e., 20 W and 30 W, about 14 W and 21 W reach the applicator

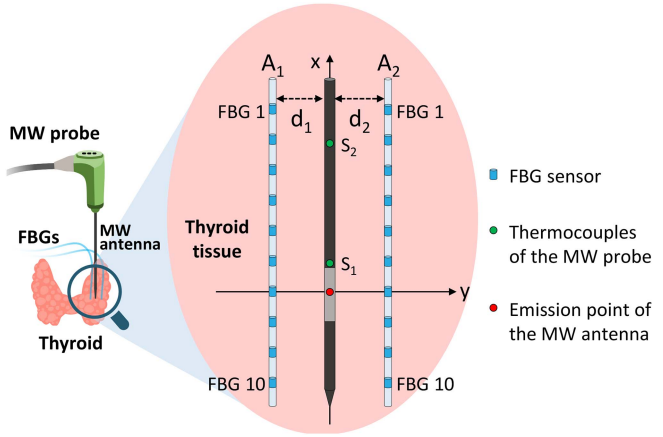

Fig. 3. Zoom on the target region of thyroid undergoing MWA showing the positioning of MW antenna and FBG arrays in the XY plane. FBGs and thermocouples are reported in blue and green, respectively, whereas the antenna emission point is in red.

emitting point, respectively. The generator also included the cooling system, which was based on CO_2 and helped limit the temperatures to which cables and probe were subjected. Therefore, CO_2 flowed inside the probe tip to cool the MW antenna. Indeed, the pressure drop induced the gas to expand, causing the probe cooling in the wake of the Joule-Thompson effect. The probe, connected to both generator and cooling system, delivered the MW energy through the emission point of the antenna, at 10 mm from the tip. An antenna having a length of 15 cm and a diameter of 17 gauge was selected because of its small size, advantageous feature given the small dimensions of the thyroid. The employed model, indeed, has been selected for its particularly small dimension of the antenna. It has been developed with the aim to treat small ablation targets, being able to quickly heat the tissue surrounding the tip and, at the same time, reduce the thermal damage extension within the longitudinal section of the ablation volume [36]. Therefore, this work aims to investigate the suitability of microwave applicator for ablating small targets as thyroid. Furthermore, the probe embedded two thermocouples. Such sensors, placed at 14 mm and 24 mm from the antenna tip, are denoted herein by S_1 and S_2, respectively (see Fig. 3).

The optical equipment is displayed in the middle left of Fig. 2 and included FBG sensors, optical interrogation unit, and laptop. Starting from the sensors, two optical fibers, each one embedding an array of ten bare FBGs produced by AtGrating Technology, were employed, as mentioned in the previous section. The FBG arrays were inserted in the thyroid tissue on either side of the probe as represented in the schematic of Fig. 3.

It is worth noting that the schematic reported in Fig. 3 is not to scale for the sake of clarity, since the fiber optics have a much smaller size, i.e., a diameter of 125 µm (bare optical fiber diameter) in correspondence of the gratings. The arrays were denoted by A_1 and A_2, whereas the FBGs were numbered from 1 to 10 as the fiber tip approached. The insertion depth of the arrays into the tissue was controlled by means of a reference marker on each optical fiber, in such a way as to place the seventh

TABLE I
DISTANCES BETWEEN FBG ARRAYS AND MW ANTENNA

Array distance from antenna	MWA test									
	1	2	3	4	5	6	7	8	9	10
d_1 [mm]	4.31	4.86	4.87	7.80	4.00	4.62	4.44	5.82	4.70	4.80
d_2 [mm]	4.94	4.21	4.92	4.80	4.80	3.96	4.70	5.15	5.50	6.40

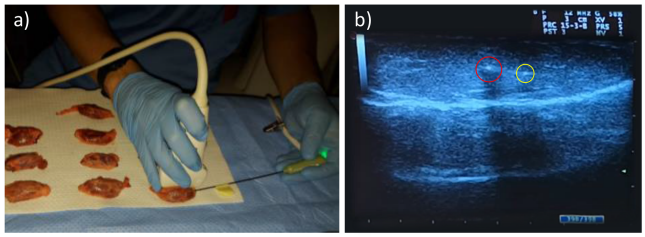

Fig. 4. Photo during the guided insertion of the MW probe inside one of the thyroid samples (a) and an ultrasound image of the tissue transversal section containing the MW antenna and the array A_2 (b). The red and yellow circles in (b) contain the transversal sections of the antenna and A_2, respectively.

sensor, i.e., FBG 7, of both A_1 and A_2 at the same depth along the x-axis with respect to the antenna emission point, denoted by the red spot in Fig. 3. The insertion of each array inside the tissue was carried out by means of a tiny percutaneous needle: the needle was inserted under the ultrasound guidance in parallel with respect to the antenna, in the same XY plane; then, the array was inserted into the needle up to the reference mark and the needle was pulled out from the thyroid tissue. The distances d_1 and d_2 between arrays (A_1 and A_2, respectively) and antenna are reported in Table I for each performed test and were calculated by means of a digital caliper. To collect the signals recorded by the FBGs, the optical interrogation unit si255 by Micron Optics and based on Hyperion Platform was used. Such interrogator could work at an adjustable acquisition frequency, set at 100 Hz for the experiments reported herein. Data acquired by the interrogator were displayed on a laptop in real-time during the MWA tests.

Finally, the last equipment of the experimental setup lies in the ultrasound machine and probe, shown on the right in Fig. 2. These tools were employed for leading and following the insertion process of MW antenna and FBG arrays inside the thyroid samples, as shown in the photos of Fig. 4. In particular, the echograph MyLab25 X Vision by Esaote was involved and the ultrasound guidance was performed before the MW power delivery and not during the treatment, in order not to induce strain in the tissue and affect the measurements of the FBGs. Therefore, the ultrasound probe allowed to ensure proximity and alignment of the FBGs to the antenna and confirmed the distances d_1 and d_2 for each test. Fig. 4(a) shows the guidance of the ultrasound probe during the procedure of antenna insertion inside one of the thyroid lobes. Instead, Fig. 4(b) reports an ultrasound image of the tissue section displaying the relative position of array A2, which transversal section is circled in yellow, from the antenna, which section is circled in red.

III. RESULTS AND DISCUSSION

In this section, the experimental results are reported and discussed. Ten tests of MWA, each performed on a different lobe of ex vivo swine thyroid, are described in the following in terms of the observed thermal lesion and recorded temperature. Therefore, the analysis of the ablation effects as a function of the power set at the MW generator is carried out from two perspectives, i.e., by evaluating i) the size of the ablated volume and ii) the thermal profiles and maps recorded by the FBGs.

Moreover, data measured by the FBGs are compared with respect to the ones recorded by the two thermocouples embedded inside the MW probe.

A. MWA Outcomes: Analysis of the Ablated Volume

The photos of the ten thyroid lobes which underwent MWA are displayed in Fig. 5. Each sample was subjected to a single MW heating lasting 5 min. To analyze the ablation outcomes at different power values, the first five tests were performed at a power of 20 W, whereas from the sixth to the tenth the tests were performed at 30 W, as reported in Fig. 5.

In order to evaluate the ablated volume for each MWA test by varying power, the organs were cut after each treatment and the size of the transversal and longitudinal sections of ablated tissue were measured by means of a digital caliper. Indeed, the photos collected in Fig. 5 show the thyroid lobes after the MWA tests and, thus, the performed cuts are clearly visible. Once cut the tissue, the transversal and longitudinal sections of the ablated volume were discriminated by a macroscopic analysis of the tissue color, which typically changes according to the proximity to the antenna. Fig. 6 reports a schematic of the ablated volume highlighting the transversal and longitudinal sections of the ablated volume in a side view (Fig. 6(a)) and detailing the dimensions of such sections (Fig. 6(b)).

Therefore, longitudinal diameter (LD) and antero-posterior diameter (APD) were measured in the longitudinal section, whereas transverse diameter (TD) in the transversal one. Fig. 6(c) shows the measuring process of LD, TD, and APD for one of the performed tests (i.e., the seventh test). The photos reported in Fig. 6(c) also show the color change of the thyroid tissue, getting closer to the brownish grey for the tissue approaching the center of the ablation region until becoming nearly black in correspondence of the tissue immediately close to the antenna.

Table II outlines the initial temperature of the thyroid lobes (i.e., T_0), MWA setting (i.e., MW power and time of treatment), thyroid size (i.e., the lengths L_1 and L_2 defined in Fig. 5), and ablation lesion size for each performed test. Concerning the lesion size, it can be observed that by providing the measurements of LD, APD, and TRD, the ablation volume V was calculated for each trial. Table II shows that, by increasing the power from 20 W to 30 W, V tends toward an increment up to about 4.5 cm^3, which is the increase of V between test 2 (i.e., when the minimum value of V was measured) and test 8 (i.e., when the maximum value of V was measured). Moreover, for each ablated volume the shape

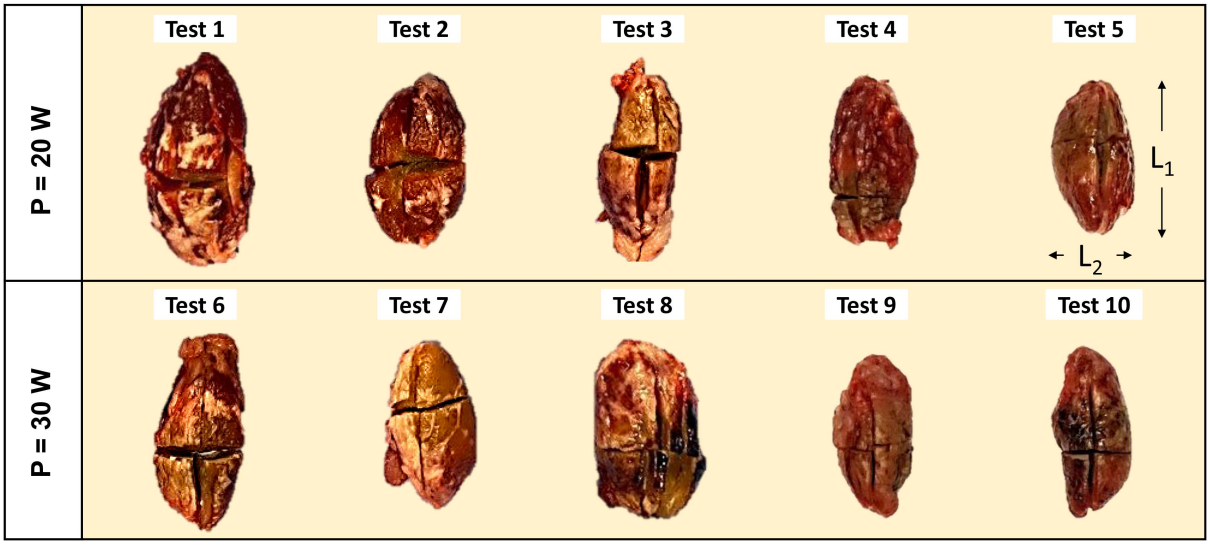

Fig. 5. Photo of the thyroid lobes undergoing MWA after each test (to scale).

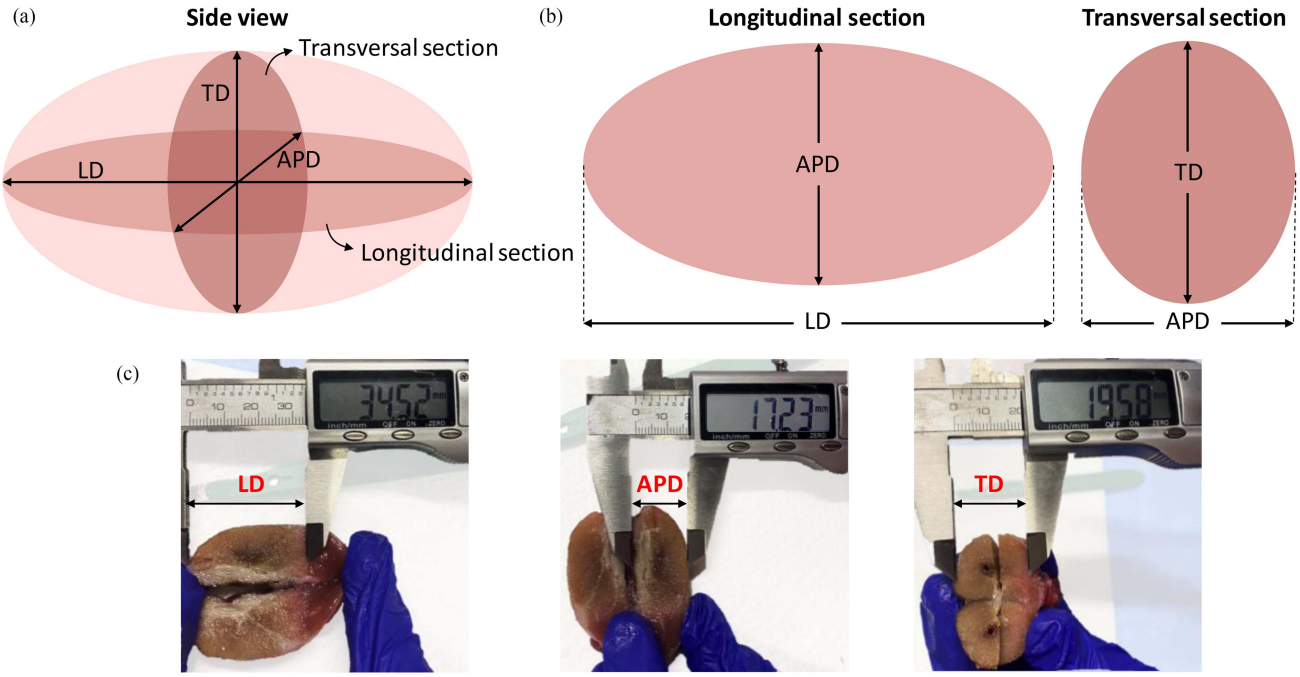

Fig. 6. (a) Side view of the ablated volume of thyroid undergoing MWA; (b) transversal and longitudinal sections of the ablated volume highlighting the diameters of the ablation lesion; (c) values of LD, APD, and TD of the lesion measured after the fifth test of MWA.

index *SI* was assessed according to the following equation [37]:

$$SI = \frac{(APD + TD)}{2LD} \tag{4}$$

Such a dimensionless parameter indicates a more spherical ablation shape as it approaches the value 1.0.

It is worth noting that ablation volume is affected by both power of the treatment and thyroid size. Indeed, dimensions of LD, ADP, and TD and, in general, *V* tend to increase by increasing the power, with fluctuations which could be due to the thyroid size.

B. MWA Outcomes: Analysis of the Temperature Recordings

For each test of MWA, temperature trends inside the target tissue as function of time and space were recorded by means of the two arrays of FBGs (i.e., A_1 and A_2).

Starting from the ΔT profiles as a function of time recorded by each FBG of the arrays, Figs. 7 and 8 report the trends measured

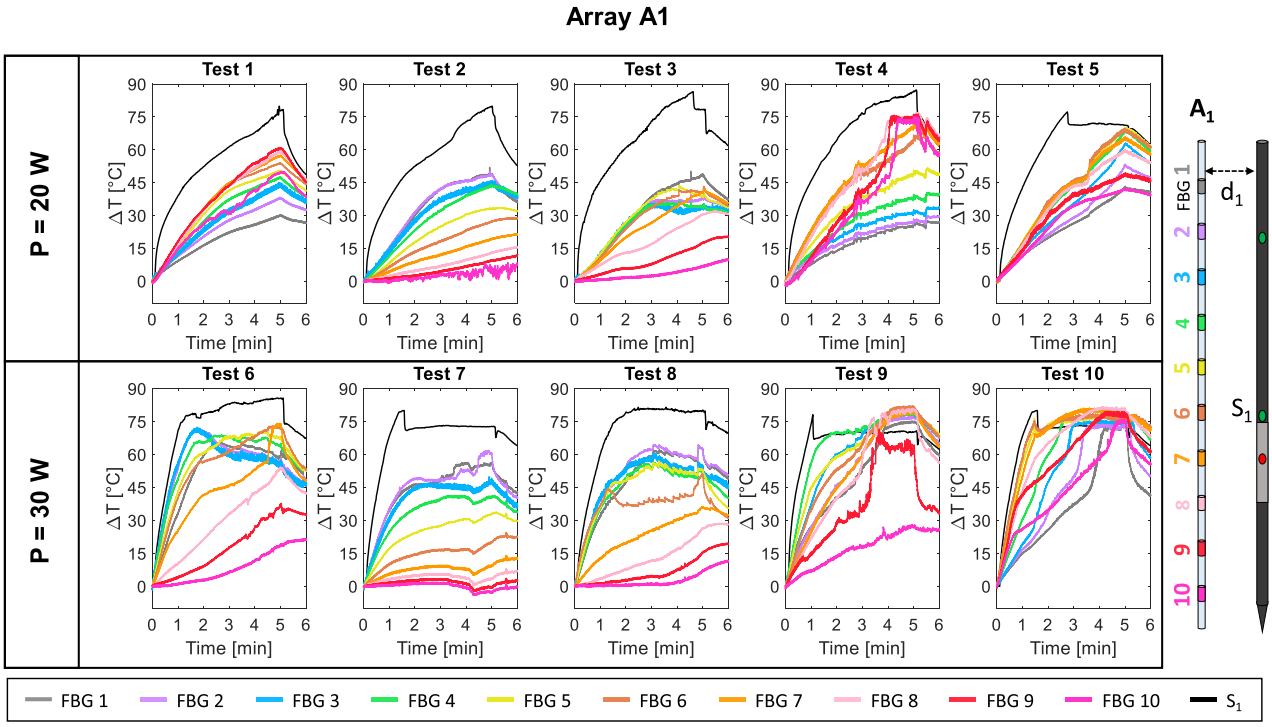

Fig. 7. ΔT profiles as a function of time recorded by array A_1 (color lines) and thermocouple S_1 (black line) during the five tests performed at 20 W (first row) and the five tests performed at 30 W (second row).

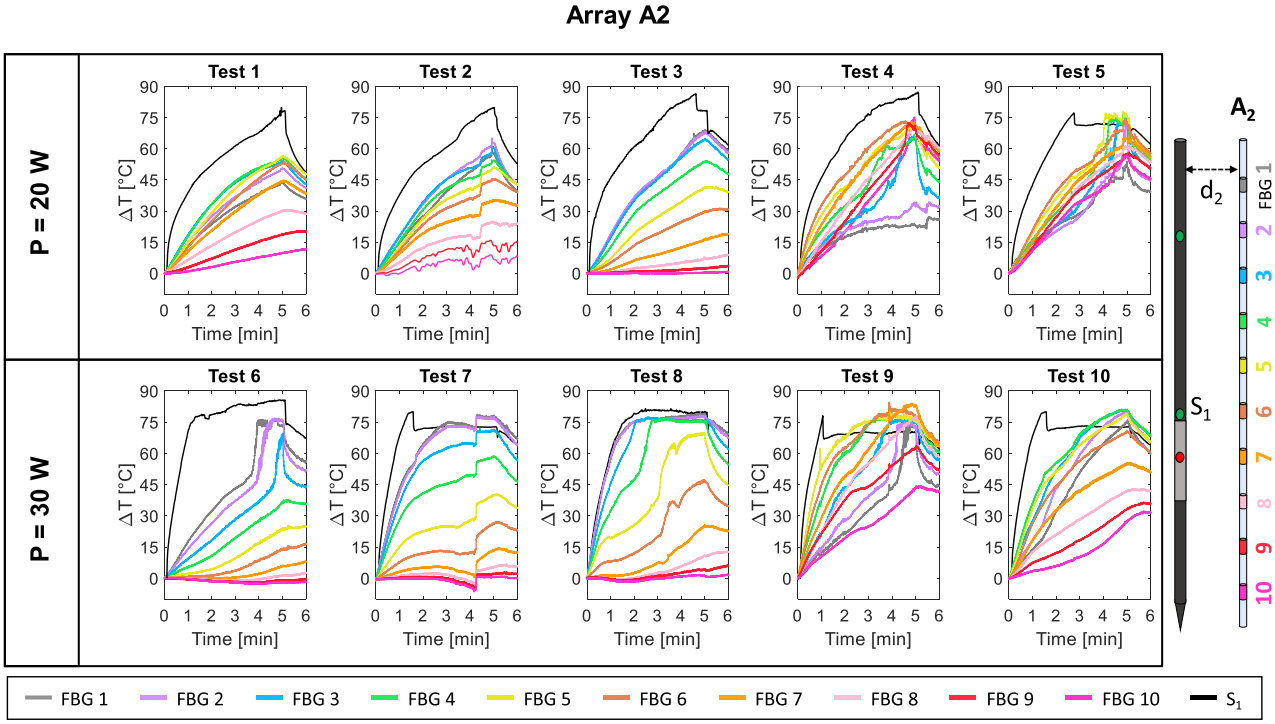

Fig. 8. ΔT profiles as a function of time recorded by array A_2 (color lines) and thermocouple S_1 (black line) during the five tests performed at 20 W (first row) and the five tests performed at 30 W (second row).

TABLE II
TREATMENT SETTINGS AND THYROID DIMENSIONS

Test	T_0 [°C]	MWA settings		Thyroid lobe size		Ablation lesion size				
		Power [W]	Time [min]	L_1 [mm]	L_2 [mm]	LD [mm]	APD [mm]	TD [mm]	V [mm^3]	SI
1	20.0	20	5	71.12	35.56	20.71	14.01	17.80	2704.19	0.77
2	20.2	20	5	52.35	32.49	21.39	15.71	14.93	2626.91	0.72
3	23.3	20	5	61.38	25.27	37.53	15.63	21.98	6750.93	0.50
4	24.0	20	5	52.79	28.67	24.40	13.35	22.34	3810.24	0.73
5	23.4	20	5	50.17	26.13	23.25	14.24	18.56	3217.43	0.70
6	20.5	30	5	61.38	28.88	28.22	15.97	24.92	5880.42	0.72
7	20.7	30	5	57.22	30.69	34.52	17.23	19.58	6097.72	0.53
8	22.1	30	5	55.96	32.49	34.49	17.46	22.57	7116.52	0.58
9	24.0	30	5	51.82	25.36	33.86	15.29	16.69	4524.28	0.47
10	24.7	30	5	56.23	27.23	27.26	15.52	19.26	4266.51	0.64

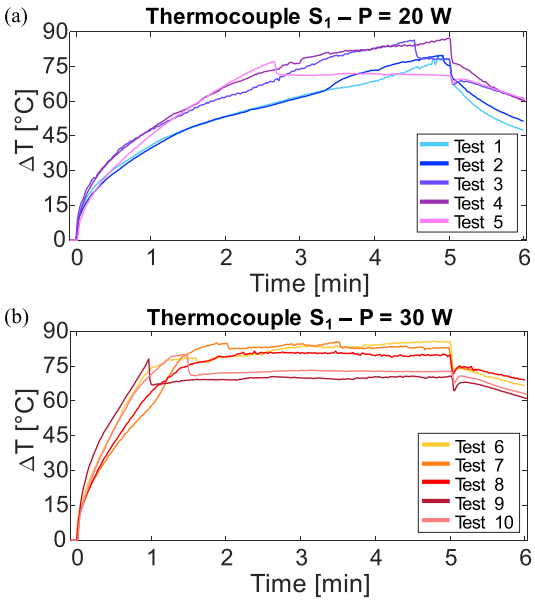

Fig. 9. ΔT profiles as a function of time recorded by the thermocouple S_1 during the tests performed at (a) 20 W and (b) 30 W .

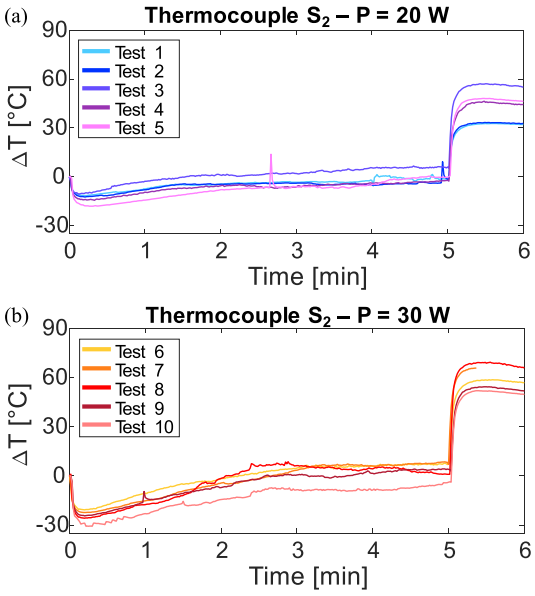

Fig. 10. ΔT profiles as a function of time recorded by the thermocouple S_2 during the tests performed at (a) 20 W and (b) 30 W .

by A_1 and A_2, respectively, highlighting the differences caused by the two involved power values, i.e., 20 W for the first row and 30 W for the second row of both Figs. 7 and 8. Indeed, by increasing the power from 20 W to 30 W, it is observable an increase of i) the maximum recorded ΔT and ii) the slope of the ΔT trend. More specifically, the maximum values of ΔT (i.e., ΔT_{max}) for each test performed at 20 W ranged from 60.9 °C to 70.9 °C, whereas ΔT_{max} recorded during the tests performed at 30 W ranged from 76.9 °C to 84.7 °C. Therefore, the FBG arrays recorded an increase up to 24 °C approximately when the power increased from 20 W to 30 W. Moreover, for the tests performed at 30 W, the ΔT slope until the maximum values increased, resulting in higher recorded temperatures in shorter times, e.g., less than 2 min for test 6 (see A1 recordings, Fig. 7) and test 8 (see A1 recordings, Fig. 8).

Besides the ΔT increase in its maximum value and slope during the MW heating, when a power of 30 W was involved, a plateau phase was recorded by several FBGs. As it can be observed in Fig. 7 and in Fig. 8, such flat profiles of ΔT during the plateau concluded in correspondence of the end of the MW heating, i.e., from the fifth minute of MWA onwards, when the decreasing ΔT profile started.

For many FBGs measuring the plateau, the starting point of the flat phase started almost immediately after they recorded the maximum value of ΔT. Some examples in this regard are given by FBG 4 of A_1 during tests 6, 7, 8, and 10 (Fig. 7), and by FBGs 4 and 5 of A_1 during test 7 (Fig. 7), and FBGs 3 and 4 of A_2 during tests 8 and 9 (Fig. 8). The slope and time needed to measure the maximum ΔT, and thus the plateau, varied depending on the distance and position of the FBGs with respect to the antenna.

Other FBGs, instead, started to record a short plateau stage only near the end of the MWA heating and after a sudden change in the slope of the ΔT profile. This is the case of, for example, FBG 7 of A_1 (Fig. 7) and FBGs 1 and 2 of A_2 (Fig. 8) during the sixth test. In correspondence of these sensors, the increasing temperatures at stake propagated later resulting in a rapid ΔT increase up to 27 °C, approximately. Such phenomenon, though less noticeable, can also be observed during the other tests performed at 30 W, especially for the nineth test.

Finally, in other cases, after recording the maximum ΔT, some FBGs measure a slight decrease of ΔT before the plateau phase, e.g., FBGs 1 and 3 of A_1 during the sixth test (Fig. 7), a sign of a possible temperature propagation through the tissue toward more external and colder thyroid regions.

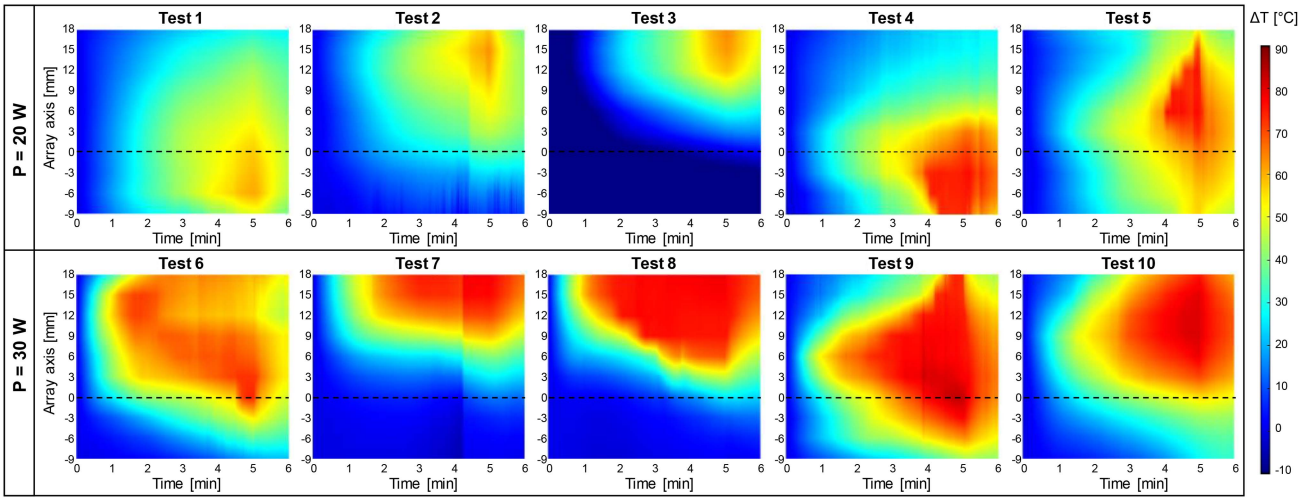

Fig. 11. Maps of ΔT as function of time for the tests performed at 20 W (first row) and at 30 W (second row) recorded by the array measuring the highest temperature values. The black dashed line refers to the theoretical position of the applicator emission point with regards to y-axis.

As previously mentioned, also temperature data recorded by the thermocouples embedded inside the MW probe were collected, as reported in Figs. 9 and 10. In particular, Fig. 9 shows the ΔT trends as a function of time recorded by S_1, which is the closest thermocouple to the emission point of the antenna, as illustrated in Fig. 3, i.e., placed at only 4 mm from it. The reported ΔT profiles were acquired during the tests performed at 20 W (Fig. 9(a)) and 30 W (Fig. 9(b)).

Due to its proximity to the emission point of the antenna, S_1 recorded higher values of ΔT with respect to the FBGs, as can be seen in Figs. 7 and 8 where the temperature measured by the thermocouple S_1 is reported in black together with the ones measured by the FBGs.

Indeed, the maximum ΔT value recorded by S_1 was 87.3 °C for the tests performed at 20 W (Fig. 9(a)), and 85.7 for the tests performed at 30 W (Fig. 9(b)). The comparison between Fig. 9(a) and (b) highlights the influence of the power settings on the temperature measurements, in particular on the ΔT slope before recording the maximum values. As for the recordings of the FBGs, when power was increased at 30 W, ΔT initial slope increased and a plateau phase was recorded until the end of the MW heating.

The close end of the MW heating corresponded to the end not only of the ΔT plateau recorded by S_1, but also of the cooling mechanism inside the MW probe. Such cooling phenomenon can be denoted in Fig. 10, which reports the ΔT profiles measured during the tests performed at 20 W (Fig. 10(a)) and the ones performed at 30 W (Fig. 10(b)), by the thermocouple S_2, placed at 14 mm from the antenna emission point. Since its location along the probe, S_2 could monitor the cool flow of CO_2 inside the MW probe, being affected more by the cooling process rather than the heat source.

Therefore, as noticeable in Fig. 10, the ΔT trends as a function of time recorded by S_2 are totally different with respect to the ones measured by the FBGs and S_1. Indeed, due to the activation of the cooling system, as MWA started, ΔT decreased in that position point. The temperature drop was more significant when power was set at 30 W, by recording –30 °C approximately. After the initial fast ΔT decrease, the temperature started to increase slightly until reaching an almost constant profile around the starting value. Then, for each test, when the MW heating ended, CO_2 flow was automatically stopped, causing a sudden increase in the ΔT recorded by S_2, denoting the significant influence of the cooling system on this thermocouple. Besides the temporal ΔT profiles, the employed arrays of FBGs allowed mapping the temperature distribution as a function of both time and space.

In this respect, Fig. 11 shows the temperature variation maps during all the tests. More specifically, the maps reported in Fig. 11 recorded by the array measuring the highest ΔT_{max}, i.e., A_1 for tests 1, 4, 6, and 10, and A_2 for the remaining ones. Such ΔT maps report the temperature values in the form of color information as a function of time, along the abscissas, and spatial position of the FBGs in the corresponding axis of the array, along the ordinates. The experimental data of ΔT measured by the FBGs belonging to the same array were interpolated by means of a piecewise linear interpolation along the ordinates, i.e., the array axis. From Fig. 11, it is visible that also ΔT maps changed their shape and values when power increased. Indeed, at 30 W, higher temperatures were recorded faster by more FBGs, being kept almost constant (tests 7 and 10) or even more increased (tests 6, 8, and 9) until the end of the MW heating, i.e., the fifth minute of MWA.

IV. Conclusion

In this study, we carried out the first research on the effectiveness of MWA in thyroid tissue by monitoring temperatures in twenty measurement points using FBGs and reconstructing the heat maps in the proximity of the MW antenna. We showed a total of ten tests at two powers (i.e., 20 W and 30 W set at the generator) for the same treatment time (i.e., 5 min) to assess the outcome (in terms of achieved temperature and necrosis volume) according to the power setting. As expected, a tendency towards an increase in ablation volume and maximum ΔT as power

rises was observed. In addition, the temperature evolution also depends on the power. Specifically, at 20 W, the temperature increased for as long as the energy was delivered. On the other hand, at 30 W, several FBGs experienced a plateau before switching off, especially the ones closest to the antenna. This finding was also confirmed by the trend of the thermocouple embedded inside the antenna in proximity to the emission point. Despite the presence of temperature plateau in temperature evolution during MWA is known, the use of arrays of FBGs allowed to measure it and quantifying this phenomenon in the area surrounding the MW applicator. Such a thermal monitoring in the target area could be relevant to adjust the clinical settings according to the desired treatment outcome. Indeed, since the thermal damage depends on temperatures recorded and exposure time, attaining cytotoxic temperatures more rapidly can decrease the treatment total duration. The real-time knowledge of the temperature distribution in the target area can assist the clinicians in developing correlations between power settings and ablation results in terms of thermal gradients and ablation dimensions.

In conclusion, these findings mark a step towards an insight into the efficacy of MWA in thyroid tissue, thus benefiting clinicians in real-world scenario.

References

[1] H. Gharib et al., "American association of clinical endocrinologists, associazione medici endocrinologi, and European thyroid association medical guidelines for clinical practice for the diagnosis and management of thyroid nodules: Executive summary of recommendations," *J. Endocrinological Investigation*, vol. 33, no. 5, pp. 287–291, May 2010.

[2] A. Faggiano, M. Del Prete, F. Marciello, V. Marotta, V. Ramundo, and A. Colao, "Thyroid diseases in elderly.," *Minerva Endocrinol.*, vol. 36, no. 3, pp. 211–231, Sep. 2011.

[3] A. El-Gammal, M. E-Balshy, and K. Zahran, "Relationship between thyroid nodule size and incidence of thyroid cancer," *Menoufia Med. J.*, vol. 32, no. 3, 2019, Art. no. 1142.

[4] L. Hegedüs, "The thyroid nodule," *New England J. Med.*, vol. 351, no. 17, pp. 1764–1771, Oct. 2004.

[5] T. E. Angell et al., "Differential growth rates of benign vs. malignant thyroid nodules," *J. Clin. Endocrinol. Metab.*, vol. 102, no. 12, pp. 4642–4647, Dec. 2017.

[6] C. Durante et al., "The natural history of benign thyroid nodules," *J. Amer. Med. Assoc.*, vol. 313, no. 9, Mar. 2015, Art. no. 926.

[7] R. A. Dedivitis, F. T. Aires, and C. R. Cernea, "Hypoparathyroidism after thyroidectomy," *Curr. Opin. Otolaryngol. Head Neck Surg.*, vol. 25, no. 2, pp. 142–146, Apr. 2017.

[8] J. - P. Jeannon, A. A. Orabi, G. A. Bruch, H. A. Abdalsalam, and R. Simo, "Diagnosis of recurrent laryngeal nerve palsy after thyroidectomy: A systematic review," *Int. J. Clin. Pract.*, vol. 63, no. 4, pp. 624–629, Apr. 2009.

[9] C. Fan et al., "Risk factors for neck hematoma requiring surgical reintervention after thyroidectomy: A systematic review and meta-analysis," *BMC Surg.*, vol. 19, no. 1, Dec. 2019, Art. no. 98.

[10] R. W. Randle and S. C. Pitt, "The role of node dissection for thyroid cancer," *Adv. Surg.*, vol. 55, pp. 131–145, Sep. 2021.

[11] T. C. Huber, "Review of the korean society of interventional radiology and European thyroid association guidelines regarding the role of radiofrequency ablation for benign and malignant thyroid tumors," *Techn. Vasc. Interventional Radiol.*, vol. 25, no. 2, Jun. 2022, Art. no. 100817.

[12] H. Gharib et al., "American association of clinical endocrinologists, american college of endocrinology, and associazione medici endocrinologi medical guidelines for clinical practice for the diagnosis and management of thyroid nodules - 2016 update," *Endocr. Pract.*, vol. 22, pp. 1–60, 2016.

[13] E. Papini et al., "Minimally-invasive treatments for benign thyroid nodules: A Delphi-based consensus statement from the Italian minimally-invasive treatments of the thyroid (MITT) group," *Int. J. Hyperthermia*, vol. 36, no. 1, pp. 375–381, Jan. 2019.

[14] K. F. Chu and D. E. Dupuy, "Thermal ablation of tumours: Biological mechanisms and advances in therapy," *Nature Rev. Cancer*, vol. 14, no. 3, pp. 199–208, Mar. 2014.

[15] E. De Vita, D. L. Presti, C. Massaroni, A. Iadicicco, E. Schena, and S. Campopiano, "A review on radiofrequency, laser, and microwave ablations and their thermal monitoring through fiber Bragg gratings," *iScience*, vol. 26, no. 11, Nov. 2023, Art. no. 108260.

[16] M. Ahmed, C. L. Brace, F. T. Lee, and S. N. Goldberg, "Principles of and advances in percutaneous ablation," *Radiology*, vol. 258, no. 2, pp. 351–369, Feb. 2011.

[17] E. M. Knavel and C. L. Brace, "Tumor ablation: Common modalities and general practices," *Techn. Vasc. Interventional Radiol.*, vol. 16, no. 4, pp. 192–200, Dec. 2013.

[18] K. B. Gala, N. S. Shetty, P. Patel, and S. S. Kulkarni, "Microwave ablation: How we do it?," *Indian J. Radiol. Imag.*, vol. 30, no. 02, pp. 206–213, Apr. 2020.

[19] C. J. Simon, D. E. Dupuy, and W. W. Mayo-Smith, "Microwave ablation: Principles and applications," *RadioGraphics*, vol. 25, no. suppl_1, pp. S69–S83, Oct. 2005.

[20] J. A. Pearce, "Models for thermal damage in tissues: Processes and applications," *Crit. Rev. Biomed. Eng.*, vol. 38, no. 1, pp. 1–20, 2010.

[21] P. Saccomandi, E. Schena, and S. Silvestri, "Techniques for temperature monitoring during laser-induced thermotherapy: An overview," *Int. J. Hyperthermia*, vol. 29, no. 7, pp. 609–619, Nov. 2013.

[22] F. De Tommasi, C. Massaroni, R. F. Grasso, M. Carassiti, and E. Schena, "Temperature monitoring in hyperthermia treatments of bone tumors: State-of-the-art and future challenges," *Sensors*, vol. 21, no. 16, 2021, Art. no. 2542.

[23] G. Palumbo et al., "Temperature profile of ex-vivo organs during radio frequency thermal ablation by fiber Bragg gratings," *J. Biomed. Opt.*, vol. 21, no. 11, pp. 117003, Nov. 2016.

[24] E. De Vita et al., "Investigation of the heat sink effect during microwave ablation in hepatic tissue: Experimental and numerical analysis," *IEEE Sens. J.*, vol. 21, no. 20, pp. 22743–22751, Oct. 2021.

[25] S. Korganbayev et al., "Closed-loop temperature control based on fiber Bragg grating sensors for laser ablation of hepatic tissue," *Sensors*, vol. 20, no. 22, Nov. 2020, Art. no. 6496.

[26] D. L. Presti et al., "Fiber bragg gratings for medical applications and future challenges: A review," *IEEE Access*, vol. 8, pp. 156863–156888, 2020.

[27] Y. Korkusuz et al., "Thermal ablation of thyroid nodules: Are radiofrequency ablation, microwave ablation and high intensity focused ultrasound equally safe and effective methods?," *Eur. Radiol.*, vol. 28, no. 3, pp. 929–935, Mar. 2018.

[28] B. Feng et al., "Ultrasound-guided percutaneous microwave ablation of benign thyroid nodules: Experimental and clinical studies," *Eur. J. Endocrinol.*, vol. 166, no. 6, pp. 1031–1037, Jun. 2012.

[29] W. Yue et al., "Ultrasound guided percutaneous microwave ablation of benign thyroid nodules: Safety and imaging follow-up in 222 patients," *Eur. J. Radiol.*, vol. 82, no. 1, pp. e11–e16, Jan. 2013.

[30] Z. Cheng et al., "US-guided percutaneous radiofrequency versus microwave ablation for benign thyroid nodules: A prospective multicenter study," *Sci. Rep.*, vol. 7, no. 1, Dec. 2017, Art. no. 9554.

[31] D. Teng, G. Sui, C. Liu, Y. Wang, Y. Xia, and H. Wang, "Long-term efficacy of ultrasound-guided low power microwave ablation for the treatment of primary papillary thyroid microcarcinoma: A 3-year follow-up study," *J. Cancer Res. Clin. Oncol.*, vol. 144, no. 4, pp. 771–779, Apr. 2018.

[32] E. De Vita et al., "Fiber bragg gratings for temperature monitoring during thyroid microwave ablation: A preliminary analysis," in *Proc. IEEE Int. Symp. Med. Meas. Appl.*, 2022, pp. 1–6.

[33] J. Fraden, "Presence, displacement, and level," in *Handbook of Modern Sensors*, Cham, Switzerland: Springer International Publishing, 2016, pp. 335–377.

[34] A. Othonos, K. Kalli, D. Pureur, and A. Mugnier, "Fibre bragg gratings," in *Wavelength Filters in Fibre Optics*, Berlin, Germany: Springer, pp. 189–269.

[35] D. Liu and C. L. Brace, "Evaluation of tissue deformation during radiofrequency and microwave ablation procedures: Influence of output energy delivery," *Med. Phys.*, vol. 46, no. 9, pp. 4127–4134, Sep. 2019.

[36] "NeuWave medical microwave ablation system," *User Reference Manual*. Accessed: Dec. 18, 2023: [Online]. Available: https://www.jnjmedtech.com/sites/default/files/user_uploaded_assets/pdf_assets/2020-05/Certus%20140%20User%20Manuel_PL-000353%20D.1.pdf

[37] R. Liu et al., "A pilot study of the shapes of ablation lesions in the canine prostate by laser, radiofrequency and microwave and their clinical significance," *PLoS One*, vol. 15, no. 4, Apr. 2020, Art. no. e0223229.

Elena De Vita (Member, IEEE) received the M.Sc. (*cum laude*) degree in biomedical engineering from "Università Campus Bio-Medico di Roma," Rome, Italy, in 2018, and the Ph.D. degree in information and communication technology and engineering from the University of Naples "Parthenope," Naples, Italy, in 2022. She is currently a Postdoctoral Researcher with the Department of Engineering, University of Naples "Parthenope." Her research focuses on fiber optic sensors in biomedical applications.

Francesca De Tommasi (Student Member, IEEE) received the M.Sc. degree (*cum laude*) in biomedical engineering from the Università Campus Bio-Medico di Roma (UCBM), Rome, Italy, in 2020. She is currently a Postdoctoral Research Fellow with the Unit of Measurements and Biomedical Instrumentation, UCBM. Her research interests focus on developing FBG-based measurement systems for patient safety enhancement and physiological monitoring.

Carlo Altomare received the graduation degree in medicine and surgery in 2014, and the post-graduation degree in radiology in 2019. Since 2021, he has been performing clinical and research activity with the Radiology Unit, Fondazione Campus Biomedico di Roma, Rome. His research focuses on Interventional Radiology in Oncology.

Daniela Lo Presti (Member, IEEE) received the Ph.D. degree from UCBM, Rome, Itlay, in 2021. She is currently an Assistant Professor with the Unit of Measurements and Biomedical Instrumentation, UCBM, Rome, Italy. Her main research interests include the design, fabrication, and feasibility assessment of smart systems and wearables based on fiber optics for biomedical applications.

Giuseppina Pacella has been a Diagnostic and Interventional Radiologist, and a Young Medical Researcher with Campus Bio-medico University since 2019. She is focusing on the field of interventional oncology, the use of different ablation techniques for tumors treatment, and navigation systems for percutaneous CT-guided biopsies and ablation procedures. She is a Member of Cardiovascular and Interventional Radiological Society of Europe (CIRSE), European Society of Oncologic Imaging (ESOI), and Società Italiana di Radiologia Medica (SIRM).

Agostino Iadicicco is currently an Full Professor with the Department of Engineering, University of Naples Parthenope, Naples, Italy. Since 2002, his research interests has been include optoelectronics and photonics devices for sensing and communications applications. He is currently involved in the design, realization and testing of novel in-fiber devices in standard and unconventional fibers including polarization maintaining and photonic bandgap fibers. He is an Associate Editor for IEEE SENSORS JOURNAL.

Massimiliano Carassiti received the master's degree (with Hons.) in medicine and surgery in 1999 and the Ph.D. degree from the Clinical University of Navarra, Pamplona, Spain. He is currently an Anesthesiologist with the Unit of Anesthesia, Intensive Care, and Pain Management with Fondazione Policlinico Universitario Campus Bio-Medico and an Associate Professor of anesthesia with UCBM. He is also one of the co-founders of the HEREMOS spin-off. His main clinical and research interests include anesthesiology, intensive care medicine, pain medicine, and management.

Rosario Francesco Grasso is currently an Interventional Radiologist and an Associate Professor of radiology and radiotherapy with UCBM. For more than 20 years, he has been dealing with ablations in oncology, both with heat ablations (RFA, MWA) and freeze ablation (CRA), in the field of liver, kidney, lung, and bone tumors.

Carlo Massaroni (Senior Member, IEEE) received the Ph.D. degree from UCBM, Rome, Itlay, in 2017. He is currently an Assistant Professor with the Unit of Measurements and Biomedical Instrumentation, UCBM, Rome, Italy. His research interests include the design, development, and test of wearable devices and unobtrusive measuring systems for medical applications. Dr. Massaroni has been the Chair of the "Wearable Sensors" TC of the Italy Chapter of the IEEE Sensors Council since 2020.

Stefania Campopiano is currently a Full Professor with the Department of Engineering, Parthenope University of Naples, Naples, Italy. Her main research interests regard the development and practical application of fiber optic sensors for the measurement of a range of physical, chemical, and biological parameters. Important research outcomes are related to the exploitation of fiber optic sensors in different fields spanning from the structural health monitoring to the biomedical field.

Emiliano Schena (Senior Member, IEEE) received the master's degree (*cum laude*) and the Ph.D. degree in biomedical engineering from UCBM in 2009. He is currently a Full Professor with the Department of Engineering at UCBM, Rome, Italy. He has directed a number of national and international research projects. His main research interests include systems for monitoring physiological parameters, application of fiber optic sensors in medicine, and laser ablation for cancer removal.

Open Access funding provided by 'Università degli Studi di Napoli "Parthenope"' within the CRUI CARE Agreement